

Structural component fatigue analysis of a hydrogenerator rotor

Carlos Mantilla-Viveros, Andrés Felipe Cardona & Fernando Casanova

*Escuela de Ingeniería Mecánica, Facultad de Ingeniería, Universidad del Valle, Cali, Colombia. camantilla@celsia.com,
andres.cardona@correounivalle.edu.co, gonzalo.casanova@correounivalle.edu.co*

Received: January 22th, 2020. Received in revised form: June 8th, 2020. Accepted: June 24th, 2020.

Abstract

This paper presents a fatigue life calculation for the pole, rotor rim, and rotor spoke of a 100 MW hydrogenerator. The mechanical and electrical parameters were measured during unit start, with the hydrogenerator working at several power levels, and during a 100 MW load rejection. The measured loads, together with centrifugal force, gravity, and magnetic pulling force, were included in finite element models to quantify stresses. Additionally, stresses produced during overspeed, phase-to-ground failure, and phase-to-phase failure conditions were evaluated. A stress history for each element was obtained by fitting the calculated stresses with a power generation history collected hourly during one year of machine operation. Fatigue life calculation was performed by using the stress history along with the Wang-Brown multiaxial fatigue model.

It was found that the three evaluated pieces are working under an infinite life regime.

Keywords: damage; fatigue life; hydrogenerator; multiaxial stress; stress measurement.

Análisis de fatiga de los componentes estructurales del rotor de un hidrogenerador

Resumen

Este artículo presenta un cálculo de vida a fatiga para el polo, la corona y la maza rotórica de un hidro-generador de 100 MW. Se midieron parámetros mecánicos y eléctricos durante el arranque, con la máquina trabajando a varios niveles de potencia y durante un rechazo de carga desde 100 MW. Las cargas medidas, junto con la fuerza centrífuga, la gravedad y la tracción magnética fueron incluidas en modelos de elementos finitos para cuantificar esfuerzos. También se evaluaron los esfuerzos producidos durante: emalado, falla fase a tierra y falla entre fases. Se obtuvo una historia de esfuerzos acoplando los esfuerzos calculados, con la historia de generación de potencia recolectada cada hora durante un año de operación de la máquina. Se realizaron cálculos de vida a fatiga utilizando la historia de esfuerzos junto con el modelo de fatiga multiaxial de Wang-Brown.

Se encontró que las tres piezas evaluadas están trabajando bajo el régimen de vida infinita.

Palabras clave: daño; esfuerzo multiaxial; hidro-generador; mediciones de esfuerzos; vida a fatiga.

1. Introduction

To meet the real-time energy demands of a given population, hydroelectric power generation plants must operate at different power levels and even undergo several start and stop processes. This produces changes in dynamic operating conditions that create fluctuating stresses in their mechanical components. Therefore, the machines are submitted to stress cycles that are different from those

produced by steady operation at the best efficiency operating point. Due to these stress cycles, some structural elements of these machines could be operating beyond their endurance limit and may be at the risk of fatigue failure. Manufacturers in the energy business rarely share information about their designs. Additionally, it is difficult for a designer to determine precise system behavior according to where the machine will be installed in terms of starts/stops, transient phenomena due to failures, and so on, which inevitably will

occur during actual operation. In addition, the dynamics of an interconnected system will vary according to system topology, meteorological conditions, and generation plant distribution.

Many of the structural elements of the generation units are subjected to fluctuating loads because of vibrations, different power generation levels, starts/stops dependent on market demands, and transient phenomena such as load rejections, short circuits, etc. These load variations can produce fatigue failures resulting in catastrophic failure due to replacement cost and time and environmental and human risks.

Most structural and failure analyses of generator components have been performed on the shaft. Momcilovic et al. [1] reported a failure analysis of a 28 MW Kaplan shaft where fatigue cracks were detected. In addition to visual examination and material property analysis, they performed stress analysis using the finite element method (FEM) during start-and-stop cycles and during steady-state operation. They found that the combination of a high stress range and a corrosive environment at the cracked region caused failure. Another case of failure on a wind turbine shaft produced by fatigue was reported in [2]. In this case, material property analysis, analytical stress calculation, and stress concentration analysis allowed the authors to conclude that high stress concentration and scratches produced by rubbing with an annular ring were the main causes of failure. Several researchers have studied shaft torque, even under transient conditions generated during transient electrical phenomena, and have evaluated its effect on shaft fatigue [3-13].

Dorji and Ghomashchi [14] presented a literature review of failure mechanisms and focused mainly on turbines where problems such as erosion and cavitation were reported as the main cause of failure. Another review that focused on the hydroturbine fatigue failure was presented in [15], where the effects of stationary operation and transient events on fatigue were analyzed. Maekawa et al. [16] implemented a measurement system to permanently monitor operating conditions and evaluate stresses for actual loads and fatigue damage. Previous studies have evaluated the effects of operating conditions and their influence on the cumulative damage of structural elements at power generation plants. Mirandola [17] evaluated the relationship between thermal stress at different load operating conditions and fatigue life and creep phenomena in steam power units.

Stress and fatigue analyses of structural elements other than shafts are scarce in the literature. Although the stress state of a generator and the methodology needed to obtain it should be easily attained by designers, they do not always share that information with the powerplant staff. However, powerplant engineers need that information to predict the fatigue life or remaining life of their machines according to the actual operation conditions and implement more efficient monitoring, maintenance, replacement and risk management plans.

In our previous paper [18], a stress and fatigue life analysis was performed on the shaft of a 100 MW generator under actual loads. In this paper, we developed a stress

analysis using the finite element method on the remaining structural elements of the rotor of the same generator considering loads under real working conditions to obtain stresses as a function of generated power. Torque, magnetic pulling forces, centrifugal forces and the weight of the components were considered as loads on the models. Torque and axial load applied by a Francis turbine on the shaft were measured with the machine working at different power levels. Measured torques were introduced into the numerical models as one of the loads. Radial displacement of the magnetic pole with the machine stopped and working was also measured to corroborate the results of the numerical models on some of the pieces. The stresses were linked to the generation history to obtain a stress history and to perform a fatigue analysis to calculate the residual life of the structural components.

This study is relevant for generation agents who need a methodology that can be applied to estimate the remaining life of the main structural components of hydrogenerators according to their operational history to develop long-term plans for restitution according to the internal strategy and risk management system of each company.

2. Methodology

Stresses on the poles, rotor rim, and rotor spoke of a 100 MW hydrogenerator were quantified by using finite element models. The loads on the models included the torque, axial force, centrifugal load due to the rotation of the rotor, magnetic pulling force on the poles, and tangential force on the poles that counters the torque applied by the runner. To validate the pole model, air gap measurements were performed in the unit to obtain the radial displacement of the pole, and the result was compared with the radial displacement obtained from the model. The torque and the axial force were measured on the shaft of the hydrogenerator while working at different power levels. Centrifugal and magnetic pulling forces were calculated by using analytical models. To obtain a stress history of each mechanical element, calculated stresses were fit to the power generation history of the unit, which consisted of hourly data of generated active power collected during one year of plant operation. The stress history was used along with the Wang-Brown multiaxial fatigue model to estimate the fatigue life of each component.

2.1. General geometry of the rotor

The basic representation of the rotor is presented in Fig. 1. The main structural parts of the rotor are the turbine, shaft, rotor spoke, rotor rim, and magnetic poles.

2.2. Field tests

Strains on the shaft were quantified using CEA-06-250US-350 strain gauges (Micro measurements, Malvern, PA). The strain gauges deliver a voltage signal proportional to strain. The normal strain was transmitted by radio frequency

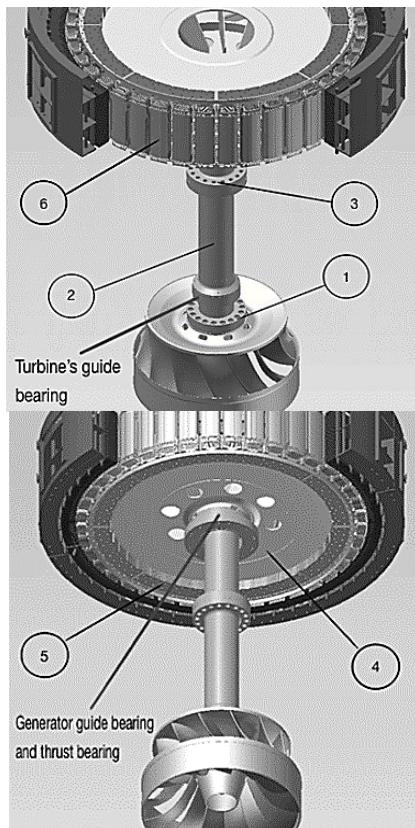


Figure 1. Rotor of the generator showing the main structural elements: 1) runner-shaft connecting bolts, 2) shaft, 3) upper-lower shaft connecting bolts, 4) rotor spoke, 5) rotor rim, and 6) magnetic pole. (Diameter of the rotor = 6.8 m).

Source: The Authors.

with a Torque Track 10K system, and the shear strain was measured with a Torque Track 9000 system (Biensfeld Engineering, Maple City, MI). The voltage signals from these torque track systems were registered using a 12-bit data acquisition system (model PMD 1280-LS, Measurement Computing, Norton, MA) at a sampling frequency of 100 Hz. To register normal strain, four strain gauges were connected in a full Wheatstone bridge configuration, with two of them aligned with the longitudinal direction of the shaft and the other two aligned at 90° . Shear strain was registered with the four strain gauges rotated 45° with respect to the longitudinal direction of the shaft. In this way, any normal strain in the longitudinal direction was cancelled, and only the principal strain produced by the torque was registered. Strains were measured with the machine working at 30, 35, 40, 50, 60, 70, 80, 90, 95 and 100 MW. Strains were also registered during machine start-up and during a 100 MW load rejection.

The air gap was measured using a General Electric measurement control system with a 3500 series Bently Nevada air gap and vibration monitoring system. This system includes four air gap 50 mm inductive sensors (Reference 13I01HAW) specially designed for large hydrogenerators. This system uses 3300 XL series vibration proximity sensors with a conversion scale of 200 mV/mil (1 mil = 0.001"). The system has a sample frequency of 20 kHz.

Signals were registered during field tests and included electrical power, angular velocity, wicket gate position, draft tube pressure pulsations, penstock pressure pulsations, temperatures, rotor field current, rotor field voltage, stator terminal current and voltage, bearing temperatures, stator temperatures and control variables of the unit (speed governor and voltage regulator). These signals were registered using a National Instruments NI cDAQ-9188 data acquisition system along with an NI 9203 analog current input module with a ± 20 mA input, 16-bit resolution, and 200 kS/s sample frequency (for field measurements, the sample frequency was set to 100 Hz) and a NI 9201 voltage input module with an ± 10 V input, 12-bit resolution and 500 kS/s sample frequency (for field measurements, the sample frequency was set to 100 Hz). The NI acquisition system was coupled with the native sensors of the unit to obtain the data during the test. All native sensors of the unit have output signals of 4-20 mA and 0-10 V.

Electrical power, angular velocity and wicket gate position are relevant to link strains with generation. Draft tube and penstock pressure pulsations were fit in the Turbine-Penstock mathematical model that was used to model the electrical torque failure at the generator's stator; they were also used to link the damage behavior of the shaft at partial load generation during low-amplitude high-cycle strain analysis (contribution of vibration at each power step to the damage in the shaft). Rotor and stator currents and voltages were needed to estimate the magnetic pull of the force component in the pole piece. All the other variables were monitored for supervision of the machine during the tests.

2.3. Model development

In this section, the geometry, loads, and boundary conditions for the numerical models of the pole, rotor rim, and rotor spoke are outlined. Simulations for the three models were performed at 60, 80, and 100 MW. Additionally, a 150% overspeed of the nominal rotation speed was simulated, which was reached by the machine after load rejection. Additionally, torques of 1.5 and 3 times the nominal torque, corresponding to phase-to-ground and phase-to-phase failure, respectively, developed in a previous study [18], were applied to the models.

2.3.1. Magnetic pole

A pole is a fundamental part of a synchronous generator; its role is to create a magnetic flux through the air gap to induce the field into the stator and allow the power flow to be transformed from its mechanical nature into electrical energy. A pole is subjected to several kinds of loads ranging from centripetal accelerations to different mechanical forces due to the change of the generated power at the plant depending on the dispatch of the unit and other forces of transient phenomena such as overspeed and electrical failure.

The body forces and surface forces acting at the pole include the magnetic pull, tangential force due to torque and centrifugal force. For this analysis, unbalanced magnetic pull was not considered.

According to [19, 20], the magnetic pull at the pole can be calculated with Maxwell's stress tensor, which is derived from the instantaneous value of the local magnetic flux density B by

$$\sigma = \frac{B^2}{2\mu_0} \quad (1)$$

Where $\mu_0 = 4\pi \times 10^{-7} H/m$ is the permeability of air.

The mean Maxwell stress in the air gap can be computed from the magnetic flux density distribution, whose values were taken from [19].

From a mathematical point of view and taking only the first harmonic, the magnetic pull is calculated as [19].

$$\bar{\sigma} = \frac{1}{2\mu_0} \frac{B_\delta^2}{\tau_p} \int_0^{\tau_p} \left(\sum_{v=1}^{\infty} \frac{B_v^F}{B_\delta} \sin\left(vx \frac{\pi}{\tau_p}\right) \right)^2 dx = \frac{B_\delta^2}{2\mu_0} \frac{1}{2} \sum_{v=1}^{\infty} \left(\frac{B_v^F}{B_\delta} \right)^2 \quad (2)$$

Where B_δ is the maximum flux density in the air gap, B_v^F is the coefficient of flux density distribution, τ_p is the polar pitch, and v is the harmonics of the induction field of the flux. For practical engineering approaches and conservative calculations, the relation $\frac{B_v^F}{B_\delta} = \frac{2}{3}$ was used [21]. According to [22], the maximum flux density was calculated as

$$B_\delta = \frac{I_{fd}\mu_0 N}{\delta} \quad (3)$$

Where I_{fd} is the rotor field current taken from the field test at different power levels, N is the number of coils at the pole (25 for this case), and δ is the air gap (14 mm for this machine).

The tangential force component can be calculated from the magnetic induction field, but based on the equilibrium principle, it can also be calculated from torque shaft measurements and by distributing the total torque into each one of the poles (40 poles) with tangential components in the opposite direction to the shaft torque direction.

The centrifugal force due to the field winding mass was obtained using Newton's second law:

$$F_c = m\omega^2 r \quad (4)$$

Where m is the mass (350 kg), ω is the angular speed (18.85 rad/s), and r is the turning radius (3.4 m).

With the previously explained loads, a 3D finite element model of the pole was developed using ANSYS v16 software, adding gravitational effects and a constant temperature of 60 degrees Celsius along the pole body, which is the average temperature reached for the pole during steady-state operation as measured after operation at 30 MW. The loads and boundary conditions implemented in the model are shown in a top view of the model in Fig. 2.

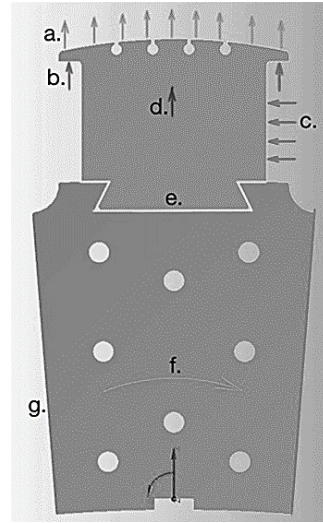


Figure 2. Top view of the 3D model of the pole (upper part) including a small portion of the rotor rim (lower part) showing the loads and boundary conditions: a) magnetic pull surface traction, b) winding centrifugal force, c) tangential force of electromagnetic torque, d) pole centrifugal force, e) friction linear model $\mu=0.2$, f) angular velocity, g) displacement boundary condition for axial symmetry (free radial displacement and total restriction for tangential displacement). The arrows at the bottom of the figure correspond to polar coordinates. Gravitational and temperature (60°C) were taken into account. The dimensions of the pole are 310 mm in the radial direction, 420 mm in the tangential direction and 1500 mm in the axial direction (long).

Source: The Authors.

In this model, a small portion of the rotor rim was simulated with tangential and axial displacement restrictions and free radial displacement to represent axial symmetry. This portion of the rotor rim was added only to allow more real boundary conditions for the pole at the dovetail surface. The results of this model are only valid for the pole piece because the symmetry condition for the rotor rim is not valid due to the presence of torque along this body.

2.3.2. Rotor rim

The rotor rim is formed by 298 plates with the geometry presented in Fig. 3. Each plate is rotated 9° with respect to the plate immediately on the top and the bottom and assembled with bolts through the holes. The assembly forms a ring with grooves on the inner diameter to be assembled with the rotor spoke and dovetail grooves on the outer diameter to hold the poles. Because the bolts restrict the displacement among plates to some degree, the analysis was performed with two models: in the first model, the ring was assumed to be a single complete body without considering the holes; in the second model, a plate including the holes was analyzed with different boundary conditions at the holes, including a) restriction of displacement at every hole, b) restriction of two holes at the sides, and c) restriction of displacement for a single hole on one side.

Fig. 4 shows a section of the model of the complete ring where the loads and boundary conditions are presented. The radial load transferred from the poles, which includes the

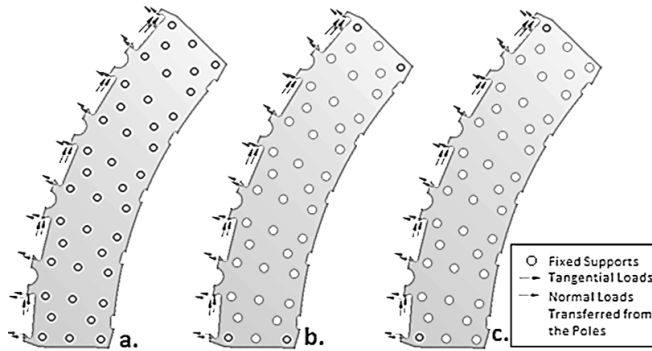


Figure 3. Rotor rim single-plate model showing boundary conditions. a) Displacement restriction on all the holes, b) displacement restriction on the two outer holes and c) displacement restriction on just one of the outer holes. The plates are 595 mm in the radial direction and 19 mm thick. Source: The Authors.

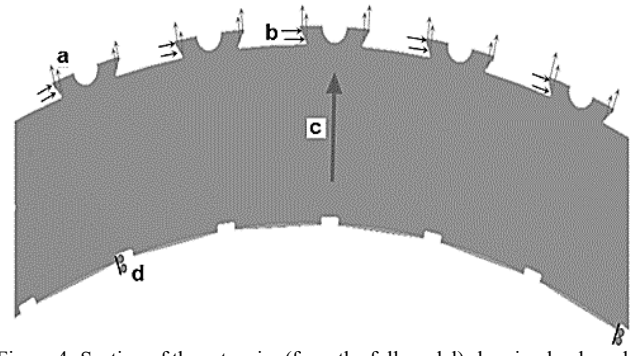


Figure 4. Section of the rotor rim (from the full model) showing loads and boundary conditions: a) radial force transferred from the poles, b) tangential force, c) centrifugal force, d) restriction of displacement in tangential direction at the keyways where the rotor rim is coupled with the rotor spoke. The external diameter of the rotor rim is 6589 mm, and the internal diameter is 5399 mm. Source: The Authors.

centrifugal force of the pole and the magnetic pull force, was applied to the dovetail surface in the radial direction (Fig. 4a). On the same surface in the tangential direction, the load equivalent to the torque was applied (Fig. 4b). The centrifugal force of the ring was also included in radial direction (Fig. 4c). The rotor rim has 40 grooves, but only eight of them are coupled to the rotor spoke. Therefore, only on eight of the 40 grooves, the restriction boundary condition was applied in the radial direction to bear the torque (Fig. 4d). Loads and boundary conditions for the second model including the holes were the same as those for the first model.

2.3.3. Rotor spoke

The rotor spoke (Fig. 5) is formed by two circular plates at the top and the bottom (Fig. 5a), eight vertical beams that work as wedges that are assembled with the keyways of the rotor rim (Fig. 5b), eight L-shaped vertical plates welded to the top and bottom circular plates that serve as structural reinforcement and work as the blades of a fan that is part of the cooling system of the machine (Fig. 5c), a ring welded to

the bottom plate and to the L-shaped plates (Fig. 5d), and eight tubes welded to the L-shaped plates and the upper plate (Fig. 5e). The bottom plate has holes to allow for air circulation and keyways to transfer torque from the shaft.

The loads and boundary conditions for the rotor spoke are shown in Fig. 6. The weight of the poles and rotor rim was applied to the vertical beams in the vertical direction (Fig. 6a). The weight of the rotor spoke was also considered (Fig. 6b). A tangential force equivalent to the torque was applied on the face of the wedge (Fig. 6c). The centrifugal force produced by the rotation was included as a rotational speed (Fig. 6d). The tangential displacement on the keyways was

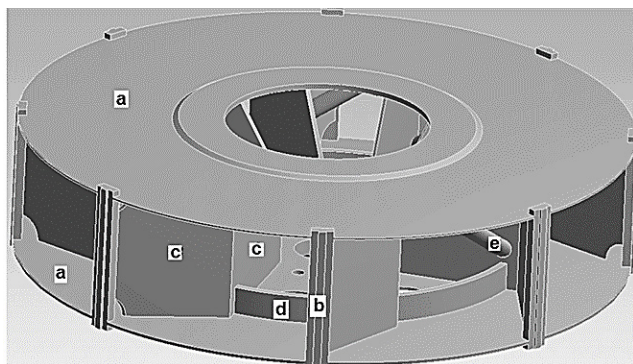


Figure 5. Geometry of the rotor spoke: a) upper and bottom circular shaft, b) vertical beams with wedges to assemble the rotor rim, c) L-shaped plates, d) rim welded to the bottom circular plate, e) tube welded to the L-shaped plate and the upper circular plate. The external diameter of the rotor spoke is 5399 mm, and the internal diameter is 700 mm. Magnetic flux density distribution in the air gap. Source: The Authors.

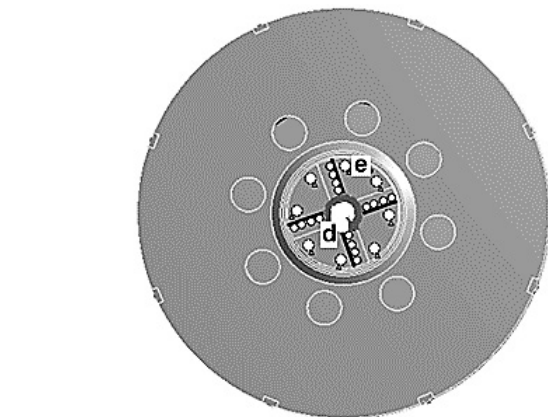
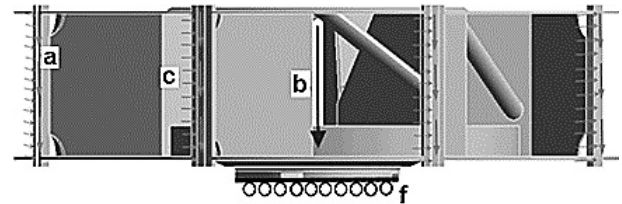


Figure 6. Loads and boundary conditions of the rotor spoke: a) weight of the poles and rotor rim, b) own weight of the rotor spoke, c) tangential load equivalent to the torque, d) angular speed of the rotor, e) restriction of displacement in tangential direction to bear the torque, f) restriction of displacement in vertical direction. Source: The Authors.

restricted to bear the torque (Fig. 6e). Finally, the displacement in the vertical direction was restricted at the region where the rim is coupled with the rotor shaft (Fig. 6f).

2.4. Fatigue analysis

First, stresses from the models were linearly interpolated to obtain the stress at power levels different from the simulated levels. Then, the generation history of the unit was obtained by compiling the operational data for one year. The information consists of hourly generation data (active power) with a resolution of 1 MW. The calculated stresses were linked to the power history to obtain a stress history.

The Wang-Brown counting method [23] was used to identify the stress reversals from the stress history. The total damage (D) produced by the stress history during the entire year was calculated by using Miner’s rule:

$$D = \sum_{i=1}^n \frac{1}{N_{fi}} \quad (5)$$

Where n is the number of cycles and N_{fi} is the fatigue life for the i – th cycle. Damage was calculated on planes ranging between $\pm 180^\circ$ with 1° of resolution. This calculation was performed using the corresponding stress components on every plane. The fatigue life for each cycle was calculated by using the Wang-Brown multiaxial fatigue model [23]:

$$\frac{\frac{\Delta\gamma_{max}}{2} + S\delta\epsilon_n}{1 + \nu' + S(1 + \nu')} = \frac{\sigma_f' - 2\sigma_{n,mean}}{E} (2N_f)^b + \epsilon_f' (2N_f)^c \quad (6)$$

Where $\Delta\gamma_{max}$ is the maximum shear strain amplitude for a given reversal (proportional and nonproportional) and $\delta\epsilon_n$ is the normal strain excursion between two turning points of the maximum shear strain computed on the maximum shear strain plane during the time between the start and end of the reversal. The S parameter is a material constant representing sensitivity to crack growth under normal strain on the maximum shear plane. Here, we used the value 1.38 reported in [23], E is the Young’s modulus, $\sigma_{n,mean}$ is the mean normal stress within the loading path, b is the strength exponent, c is the ductility exponent, σ_f' is the fatigue strength coefficient, ϵ_f' is the fatigue ductility coefficient and ν' is the effective Poisson’s ratio.

2.5. Material mechanical properties

Table 1 presents the mechanical properties taken from Ref. [24] for the international standard (SAE), which are

Table 1. Mechanical properties of the materials.

Piece	S_{ut} (MPa)	S_y (MPa)	ϵ_f'	σ_f' (MPa)	b	c
Pole	400-510	205-250	0.17	902	-0.12	-0.42
Rotor rim	400-510	205-250	0.17	902	-0.12	-0.42
Rotor spoke	671	353	0.52	1099	-0.11	-0.54

Source: The Authors.

approximated to the material specifications provided by the manufacturer.

3. Results and discussion

3.1. Stress measurement on the shaft

The measured axial and shear stresses are presented in Fig. 7 for the start of the machine, power ranging from 30 to 100 MW and during load rejection. Normal stresses during load rejection were not registered due to technical problems. The number on each step of shear stress corresponds to the respective generated power. The average torque and axial load calculated from the registered stresses are presented in Fig. 8. A more detailed description of these experimental results can be found in our previous paper [18]. Here, we only include these results because the measured average torque was applied on the models of the pole, rotor rim and rotor spoke as a load. The fluctuations of the stresses around the average value observed in Fig. 7 for each power level were not considered in the models because in our previous paper, we found that the damage produced on the shaft by the fluctuation was small in comparison with the change of power level.

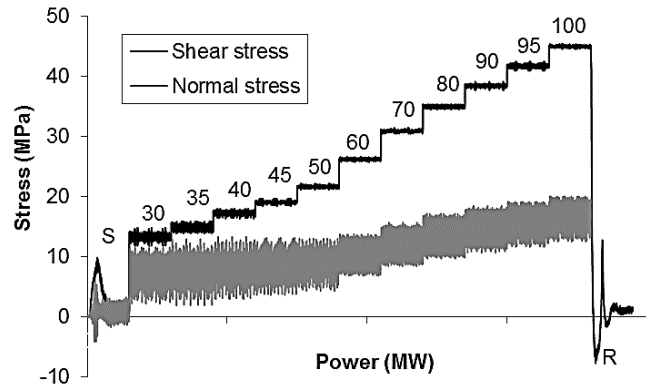


Figure 7. Shear and normal stresses with the machine working at power between 30 and 95 MW. The number on each step corresponds to the generated power in MW. S corresponds to the start of the machine, and R corresponds to load rejection.

Source: The Authors.

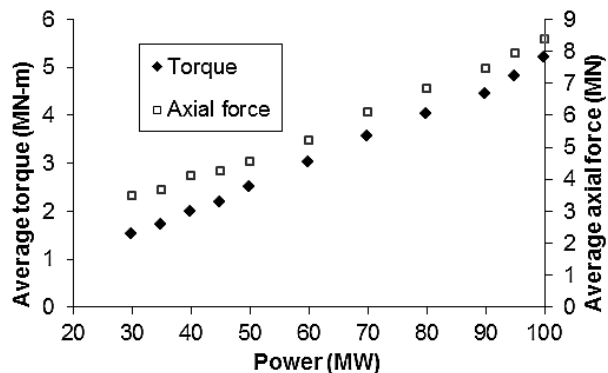


Figure 8. Average torque and axial force as a function of generated power.

Source: The Authors.

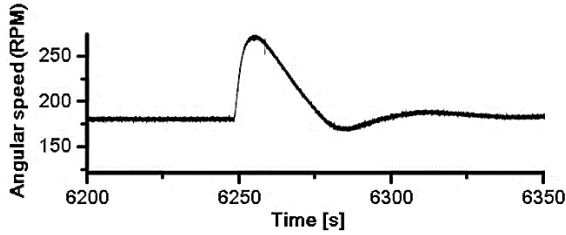


Figure 9. Rotational speed of the machine during load rejection.
Source: The Authors.

3.2. Rotational speed results

Fig. 9 shows the rotational speed of the machine during load rejection. Prior to load rejection, the machine had a rotational speed of 180 rpm. Immediately after load rejection, the speed increased to a value of approximately 270 rpm and then decreased again to the nominal speed. This increase in the speed is important because it increases the centripetal force and therefore must be included in the numerical models, especially at the poles since they are the furthest pieces from the rotation axes and thus experience the highest centripetal force.

3.3. Radial displacement measurement

The air gap measurements averaged for the four sensors are presented in Table 2 for the three tests. The radial displacement was calculated as the difference between the air gap under static conditions (14 mm) and the measured air gap under working conditions. Measurements were only performed with the machine working at 30 MW because that was the maximum generation power level allocated to the plant due to a low reservoir level caused by a dry season.

3.4. Modeling results

3.4.1. Magnetic pole

The critical point on the poles was the rounded region at the end of the dovetail (Fig. 10). Referring to a cylindrical coordinate system centered at the center of the machine, the radial stress (σ_r) and shear stress ($\sigma_{r\theta}$) are presented in Table 3 for the evaluated load cases. The other components of the stress tensor were considerably smaller. In addition to electrical failures, overspeed was found to produce an important increase in stresses. This can be explained by the location of the pole with respect to the rotor. As it is located far from the rotation axes, high centrifugal forces are produced during overspeed due to the high turning radius.

The maximum displacement at the pole obtained from the model simulated at 30 MW was 2.35 mm. This result is inside

Table 2.
Average air gap and radial displacement obtained for three tests.

Test	1	2	3
Average air gap (mm)	11.8	11.4	12.0
Radial displacement (mm)	2.2	2.6	2

Source: The Authors.



Figure 10. von Mises stress on the pole showing the critical point at the end of the dovetail.

Source: The Authors.

Table 3.
Stresses (MPa) at the root of the dovetail region of the pole for the evaluated load conditions.

Load	σ_r (MPa)	$\sigma_{r\theta}$ (MPa)
Overspeed 1.5X	172.1	90.6
60 MW	107.1	54.0
80 MW	125.5	55.7
95 MW	146.6	58.6
Ground-phase failure	206.1	65.0
Phase-phase failure	216.1	70.5

Source: The Authors.

the measured results (Table 2), which can be seen as a validation for the model.

3.4.2. Rotor rim

Two critical regions were found for the rotor rim: the rectangular grooves where the rotor spoke is assembled (Fig. 11a) and the dovetail where the pole is assembled (Fig. 11b). Greater stresses were found at the dovetail. The second model, which included the holes, showed some stress concentration at the holes, but those stresses were smaller than the stresses at the grooves shown in Fig. 11. Therefore, they were no longer considered. Table 4 presents the stresses at the dovetail for the evaluated load conditions. For the rotor rim, overspeed was found to be the more critical event because it produces the highest stresses.

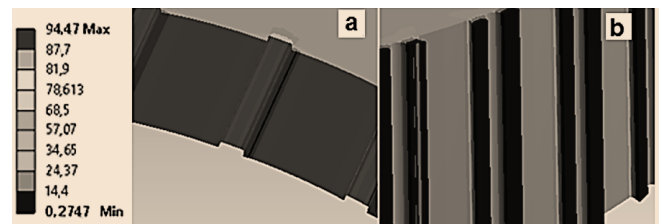


Figure 11. von Mises stress at critical points in the rotor rim: a) keyway to the rotor rim assembly with the rotor spoke, b) dovetail to the magnetic pole assembly.

Source: The Authors.

Table 4.

Stress components (MPa) at the critical points of the rotor rim for the evaluated load conditions.

Load	σ_r (MPa)	$\sigma_{r\theta}$ (MPa)
Overspeed 1.5X	163.8	56.4
60 MW	94.3	29.8
80 MW	94.5	29.9
95 MW	94.8	30.1
Ground-phase failure	98.9	31.3
Phase-phase failure	107.3	33.9

Source: The Authors.

3.4.2. Rotor spoke

Two critical regions were found at the rotor spoke: the holes of the ventilation systems (Fig. 12a) and the keyway used to transfer the torque from the shaft (Fig. 12b). However, the maximum stresses were found at the ventilation holes. Table 5 presents the stresses on the ventilation holes. In the rotor spoke, the stresses were strongly dependent on the power level and the torque produced during failures created a notable increase in stresses. In contrast with the pole and rotor rim, rotational speed did not affect stresses in a notable way. This result is reasonable since the relative location of the poles is opposite to the critical region of the rotor spoke; the ventilation holes are close to the rotation axes, while poles are at the furthest location. Additionally, it is important to note that the rotor rim does not transfer radial loads to the rotor spoke because the rectangular grooves transfer only tangential load.



Figure 12. Regions with maximum von Mises stresses at the rotor spoke: a) holes used for ventilation at the bottom of the rotor spoke, b) keyway at the bottom of the rotor spoke with the wedge used to transfer torque from the shaft.

Source: The Authors.

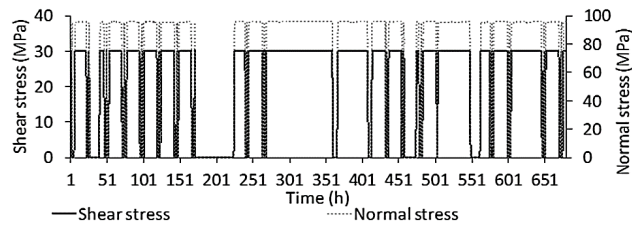


Figure 13. Stress history at the dovetail of the pole during one month of normal operation.

Source: The Authors.

3.5. Fatigue life

Stresses obtained for the evaluated power levels for every mechanical element were interpolated to obtain the stresses at every power level in the generation history. With the interpolated stresses and the generation history, a stress history was obtained for every element. As an example, Fig. 13 shows a stress history during one month obtained for the dovetail of the pole.

The calculated damage at the pole under normal operation for one year is presented in Fig. 14. In the same figure, the damage produced by one phase-to-phase failure and the total damage (normal operation plus one failure) are presented.

With the damage obtained for normal operation, the estimated fatigue life was 91240 years. Including one phase-to-phase failure, the life was reduced in only 83 years, which means a small influence of this failure on fatigue life. Similar results were obtained for phase-to-ground failure and overspeed.

Damage at the dovetail of the rotor rim under normal operation and including one phase-to-phase failure is presented in Fig. 15. With the calculated damage, under normal conditions, the estimated fatigue life was 2.3 million years. The inclusion of one phase-to-phase failure reduced the life in 1671 years. Similar results were found for ground-to-phase failure and overspeed.

Table 5.

Stress components in MPa at the critical points of the rotor spoke for the evaluated load conditions.

Load	σ_r (MPa)	$\sigma_{r\theta}$ (MPa)
Overspeed 1.5X	42.5	39.4
60 MW	45.8	42.7
80 MW	57.7	53.9
95 MW	69.7	65.0
Ground-phase failure	232.7	217.3
Phase-phase failure	572.6	534.8

Source: The Authors.

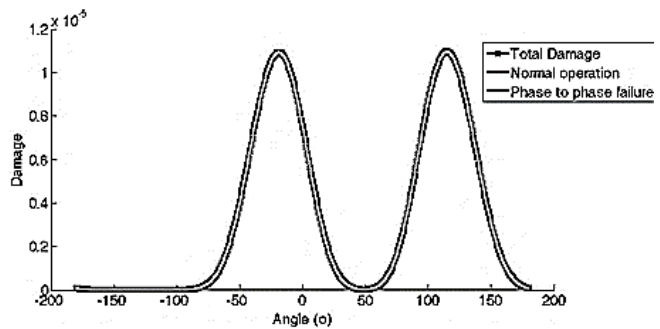


Figure 14. Damage produced at the dovetail of the pole under normal operation and including one phase-to-phase failure. The maximum damage was found at a plane rotated 115° with respect to the polar coordinate system shown in Fig. 2.

Source: The Authors

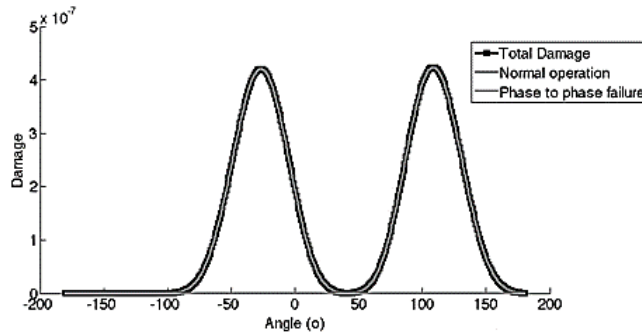


Figure 15. Damage at the rotor rim dovetail for one year of normal operation and with one phase-to-phase failure. The maximum damage was located at an angle of 108 degrees with respect to the polar coordinate system.

Source: The Authors

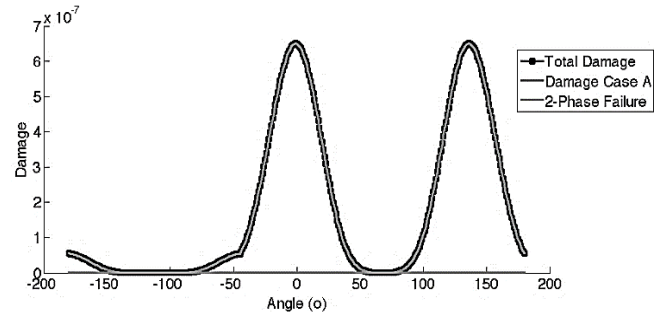


Figure 16. Damage at the ventilation holes of the rotor spoke produced under normal operation and including one phase-to-phase failure. The maximum damage was located at 136° with respect to the polar coordinates.

Source: The Authors

Damage at the ventilation holes of the rotor spoke under normal operation and with one phase-to-phase failure is presented in Fig. 16. The calculated life under normal operation was 1.539 million years. The inclusion of one phase-to-phase failure subtracts 5665 years of fatigue life.

Table 6 summarizes the fatigue life obtained for the three analyzed elements under the four working conditions. These results indicated that the three elements are practically working under an infinite life regime. However, these results have to be improved by including the actual mechanical properties of the materials for each of the studied elements since in this study, mechanical properties taken from the literature were used. Additionally, the corrosion rate and temperature should be included as well as strain measurements at the rotor spoke, rotor rim and pole to cover the vibration contribution in the fatigue damage study.

Special attention should be paid to the case of the rotor spoke since it includes welding for joining its different parts. In this study, the fatigue life of the ventilation holes where numerical models showed important stresses was analyzed. However, even if welding presents smaller nominal stresses around it, its fatigue life should be analyzed based on the experimental data of fatigue life for joints with similar configurations. To achieve this, stress measurements around the welds may be needed to perform an analysis by using the nominal stress approach [25]. However, stress measurements inside the rotor may be challenging since a magnetic field might affect the strain gauge signals.

4. Conclusions

Stresses at the dovetail of the pole and the rotor rim were strongly affected by the overspeed of the machine. On the other hand, overspeed did not affect stresses on the ventilation hole of the rotor spoke where stresses were more affected by electrical failures.

With the mechanical properties borrowed from the literature, it was found that the piece with the shortest fatigue life is the pole. However, even this element was found to be working at an infinite life regime.

Table 6.

Fatigue life (years) for the three analyzed elements under the four working conditions.

	NO*	Overspeed	PGF**	PPF***
Pole	91240	91157	91240	91157
Rotor rim	2.36E+06	2.35E+06	2.35E+06	2.35E+06
Rotor spoke	1.539E+06	1.539E+06	1.539E+06	1.539E+06

* Normal operation, ** Phase-to-ground failure, *** Phase-to-phase failure
Source: The Authors.

Further research is needed to determine the actual mechanical properties of the elements and quantify the stresses close to welds in the rotor spoke to improve the fatigue life estimation.

Acknowledgement

This work was supported by vicerrectory of research from Universidad del Valle, grant number CI 806. Authors also thank EPSA (Empresa de Energia del Pacifico) for the support given to this research.

References

- [1] Moncilovic, D., Odanovic, Z., Mitrovic, R., Atanasovska, I. and Vuherer, T., Failure analysis of hydraulic turbine shaft, *Engineering Failure Analysis*, 20, pp. 54-66, 2012. DOI: 10.1016/j.engfailanal.2011.10.006
- [2] Zhang, Z., Yin, Z., Han, T. and Tan, A., Fracture analysis of wind turbine main shaft, *Engineering Failure Analysis*, 34, pp. 129-139, 2013. DOI: 10.1016/j.engfailanal.2013.07.014
- [3] Chyn, C., Wu, R.C. and Tsao, T.P., Torsional fatigue of turbine-generator shaft owing to network faults, *IEEE Proc. Gener. Transm. Distrib.*, [online]. 143(5), pp. 479-486, 1996. Available at: <https://ieeexplore.ieee.org/stamp/stamp.jsp?tp=&arnumber=543374>
- [4] Joyce, J.S. and Kulig, T., Torsional fatigue of turbine-generator shaft caused by different electrical system faults and switching operations, *IEEE Transactions on Power Apparatus and Systems*, [online]. PAS-97(5), pp. 1965-1977, 1978. Available at: <https://ieeexplore.ieee.org/stamp/stamp.jsp?tp=&arnumber=4181641>
- [5] Mitsche, J.V. and Rusche, P.A., Shaft torsional stress due to asynchronous fault synchronization, *IEEE Transactions on Power Apparatus and Systems*, [online]. PAS-99(5) pp. 1864-1860, 1980. Available at: <https://ieeexplore.ieee.org/stamp/stamp.jsp?tp=&arnumber=4114007>

- [6] Joyce, J.S. and Lambrecht, D., Status of evaluating the fatigue of large steam turbine-generator caused by electrical disturbances, *IEEE Transactions on Power Apparatus and Systems*, [online]. PAS-99(1), pp.111-119, 1980. Available at: <https://ieeexplore.ieee.org/stamp/stamp.jsp?tp=&arnumber=4113775>
- [7] Ahlgreen, L., Johansson, K.E. and Gadhammar, A., Estimated life expenditure of turbine-generator shafts at network faults and risk for sub synchronous resonance in the Swedish 400 KV system, *IEEE Transactions on Power Apparatus and Systems*, PAS-97(6), pp. 2005-2018, 1978.
- [8] Hammons, R.J., Effect of fault clearing and damper modeling on excitation and decay of vibrations in generator shafts following severe disturbances on the system supply, *IEEE Transactions on Energy Conversion*, [online]. EC-2(2), pp. 308-320, 1987. Available at: <https://ieeexplore.ieee.org/stamp/stamp.jsp?tp=&arnumber=4765846>
- [9] Rusche, P.A., Katsiapis, Z.A. and Triesenberg, D.M., Turbine-Generator shaft related system planning criteria, operating experiences and selected study results, *IEEE Transactions on Power Apparatus and Systems*, [online]. PAS-99(6), pp. 2153-2163, 1980. Available at: <https://ieeexplore.ieee.org/stamp/stamp.jsp?arnumber=4114053>
- [10] Bovsunovsky, A.P., Fatigue damage of steam turbine shaft at asynchronous connections of a turbine generator to electrical network, *Journal of Physics: Conference Series*, 628, in: 11th International Conference on Damage Assessment of Structures (DAMAS 2015) 24–26 August 2015, Ghent, Belgium, 2015. DOI: 10.1088/1742-6596/628/1/012001
- [11] Liu, C., Jiang, D. and Chen, J., Coupled torsional vibration and fatigue damage of turbine generator due to grid disturbance, *Journal of Engineering for Gas Turbines and Power*, 136(6), art 062501, 2014. DOI: 10.1115/1.4026214
- [12] Chen, D., Zhang Y. and Gu, Y., Online evaluation of turbo-generator shaft fatigue damage caused by subsynchronous oscillation, *IEEE Access*, 8, pp. 55342-55353, 2020. DOI: 10.1109/ACCESS.2020.2981509.
- [13] Li, R., Zhao, S., Gao, B., Zhang, R. and Hu, Y., Subsynchronous torsional interaction of steam turbine under wind power oscillation in wind-thermal power bundled transmission system, *Electrical Power and Energy Systems*, 108, pp. 445-455, 2019. DOI: 10.1016/j.ijepes.2019.01.007
- [14] Dorji, U. and Ghomashchi, R., Hydro turbine failure mechanisms: an overview, *Engineering Failure Analysis*, 44, pp. 136-147, 2014. DOI: 10.1016/j.engfailanal.2014.04.013
- [15] Liu, X., Lou, Y. and Wang, Z., A review on fatigue damage mechanism in hydro turbines, *Renewable and Sustainable Energy Reviews*, 54, pp. 1-14, 2016. DOI: 10.1016/j.rser.2015.09.025
- [16] Maekawa, O., Kanazawa, Y., Takahashi, Y. and Tani, M., Operating data monitoring and fatigue evaluation systems and findings for boiling water reactors in Japan, *Nuclear Engineering and Design*, 153, pp. 135-143, 1995. DOI: 10.1016/0029-5493(95)90005-5
- [17] Mirandola, A., Stoppato, A. and Castro, E., Evaluation of the effects on the operation strategy of a steam power plant on the residual life of its devices, *Energy*, 35, pp. 1024-1032, 2010. DOI: 10.1016/j.energy.2009.06.024
- [18] Mantilla, C.A. Valdés, J.A. and Casanova, F., Multiaxial fatigue analysis for the shaft of a 100 MW hydro-power generator, *Journal of Mechanical Engineering and Sciences*, 13(2), pp. 4928-4945, 2019. DOI: 10.15282/jmes.13.2.2019.12.0409
- [19] Traxler-Samek, G., Tutorial: calculation of the magnetic pull of hydrogenerators. Hydro Generator Technology Center, Alstom, Switzerland, 2006.
- [20] Pyrhönen, J., Jokinen, T. and Hrabovcová, V., Design of rotating electrical machines, John Wiley & Sons, United Kingdom, 2008.
- [21] Rosenberg, E., Magnetic pull in electric machines, AIEE. 1918.
- [22] Kostenko, M.P. and Piotrovski, L.M., Máquinas eléctricas II. Editorial MIR, Moscú, 1976.
- [23] Wang, C.H. and Brown, M.W., Life prediction techniques for variable amplitude multiaxial fatigue – Part 1: theories, *Journal of Engineering Materials and Technology*, 118, pp. 367-370, 1996.
- [24] Boardman, B., Fatigue resistance of steels. *ASM Handbook, Vol. 1: Properties and selection: irons, steels, and high-performance alloys*. ASM Handbook Committee, 1990, pp. 673-688.
- [25] Stephens, R.I., Fatemi, A., Stephens, R.R. and Fuchs, H.O., *Metal fatigue in engineering*, 2nd ed., John Wiley & Sons, INC, New York, 2001.

Carlos Mantilla-Viveros, received the BSc. Eng in Mechanical Engineering in 2009 and the MSc. in Engineering in 2016 both from the Universidad del Valle, Cali, Colombia. From 2007 to the present he is working at CELSIA as the chief of the technical management for hydro and wind technologies. He is also professor in Electrical Engineering Department at Universidad del Valle, Colombia. His research interest includes: Fatigue and fracture of mechanical systems and control and transient phenomena for hydraulic and wind generation
ORCID: 0000-0003-2663-4557

Andres Felipe Cardona, received the BSc. Eng in Mechanical Engineering in 2016 from Universidad del Valle, Colombia. Currently he is a Design Engineer in OPT Ingeniería S.A.S. His role involves CFD and FEA Analysis for Water Treatment Equipment.
ORCID: 0000-0002-0951-0854

Fernando Casanova, received the BSc. Eng in Mechanical Engineering in 2003 and the MSc in Mechanical Engineering in 2006, all of them from the Universidad del Valle, Colombia. In 2013 he received the PhD in Mechanical Engineering from the University of Florida (USA). Currently he is a full professor in Mechanical Engineering Department at Universidad del Valle.
ORCID: 0000-0002-3146-2027